Paleoclimate records reveal elusive 200-kyr eccentricity cycle for the first time

Frits Hilgen, Christian Zeeden, Jacques Laskar

Global and Planetary Change 194 (2020) 103296

Contents lists available at ScienceDirect

Global and Planetary Change

journal homepage: www.elsevier.com/locate/gloplacha

Invited research article

Paleoclimate records reveal elusive ~200-kyr eccentricity cycle for the first time

Frits Hilgen[a,*], Christian Zeeden[b,1], Jacques Laskar[b]

[a] Department of Earth Sciences, Utrecht University, Princetonlaan 8a, 3584 CB Utrecht, the Netherlands
[b] IMCCE, Observatoire de Paris, 77 Avenue Denfert-Rochereau, Paris, France

ARTICLE INFO

Keywords:
Paleoclimate
Milankovitch cycles
200-kyr eccentricity cycle
Astronomical solution
Higher-order terms

ABSTRACT

The main cycles of Earth's eccentricity as recorded in paleoclimate archives signify 2nd order terms, combining two g-frequencies associated with the precession of perihelia of the inner planets and Jupiter. However, many weaker cycles are present and may be documented as well. Here we report on a thus far unnoticed ~200-kyr cycle observed in rhythmically bedded marine marls and limestones of early Paleocene age in NE Spain and adjacent France. This cycle is expressed as alternating distinct and less distinct ~100-kyr $CaCO_3$ maxima and associated magnetic susceptibility (MS) minima, which correspond to successive minima of the short ~100-kyr eccentricity cycle.

The most plausible explanation is that this ~200-kyr cycle represents a weak but real cycle in eccentricity. Due to its weakness, this cycle is only expressed as alternatingly strong and weak ~100-kyr minima in eccentricity time series, a pattern that is identical to what we observe in the proxy records and outcrop. Its origin as eccentricity cycle is complex as it is composed of 4 to 6 individual components. A simplified solution solely based on the five leading g-frequencies reveals that most of these components originate from combinations of these 5 frequencies. However, they do not correspond to 2nd order terms, which underlie the principal short and long eccentricity cycles, but to much weaker higher order terms. Three of them have been identified as 4th order terms and two as 6th order terms, representing combinations of 2nd order terms, such as the first harmonic, 2(g2 – g5), of the 405-kyr cycle and related components.

It is for the first time that the combined effect of such weak components has been identified in paleoclimatic records, which is only possible because they are not overwhelmed by much stronger 2nd order terms in this frequency band. Finally, the typical pattern that results from interference with the much stronger ~100-kyr cycle might be used as a template for testing the accuracy of astronomical solutions in the future.

1. Introduction

The astronomical theory of climate change starts from the notion that insolation received at the top of Earth's atmosphere varies in harmony with quasi-periodic changes in Earth's orbital and inclinational parameters, namely eccentricity with principal periods of ~100- and 405-kyr, axial inclination or obliquity with a dominant period of 41-kyr and climatic precession with main periods of 19- and 23-kyr. These cycles are primarily caused by gravitational perturbations by the planets and the Moon (e.g., Milankovitch, 1941) and the multitude of their components is connected with three fundamental frequencies, two of which are loosely connected with the planets, namely the g- and s-frequencies, which describe the precessional motions of their perihelia (g) and nodes (s), and astronomical precession (with a frequency p termed the precession constant), which is associated with the Earth-Moon system (Laskar et al., 2004; Hinnov, 2000). The leading eccentricity terms can all be written as a combination of two g-frequencies, while the main climatic precession and obliquity terms can be written as combinations of respectively a single g and s frequency, and p. The origin of the main frequency components of precession, obliquity and eccentricity recorded in our paleoclimate archives are invariably related to the rocky planets and the innermost outer gas giants of Jupiter and Saturn, as these planets exert the largest gravitational pull on Earth (Laskar et al., 2004; Hinnov, 2000). However, many more components are present in the solution (Laskar et al., 2004), but these are generally too weak to be detectable in paleoclimatic archives, which are often noisy and distorted in the stratigraphic domain (e.g., Hilgen et al., 2015a). For instance, cycles having a less familiar period close to ~200-

* Corresponding author.
E-mail address: F.J.Hilgen@uu.nl (F. Hilgen).
[1] Now at: LIAG – Leibniz Institute for Applied Geophysics, Geozentrum Hannover, Hannover, Germany.

https://doi.org/10.1016/j.gloplacha.2020.103296
Received 14 March 2020; Received in revised form 11 August 2020; Accepted 18 August 2020
Available online 26 August 2020

kyr have been documented in paleoclimate archives. Up to now these have been attributed to the 173-kyr modulation cycle of obliquity (associated with s3 – s6, number refers to the planet in order of distance from the Sun) (Beaufort, 1994; Westerhold et al., 2005; Boulila et al., 2018) or are explained as harmonic of the 405-kyr cycle or "double" ~100-kyr cycle that result from non-linear responses of the climate system to the main eccentricity components (Hilgen et al., 2015; Liebrand et al., 2016).

In this paper, we report on a ~200 kyr cycle with a different origin. This cycle is detected in climatic proxy records of rhythmically bedded deep marine limestones and marls of the Danian Limestone Formation of early Paleocene age in the Zumaia and Hendaye sections. We argue that the cycle exemplifies a real but weak eccentricity component that is related to higher 4th and 6th order terms in eccentricity, which are much weaker than the 2nd terms that underlie the main cycles, such as the long 405-kyr and the short ~100-kyr eccentricity cycle. First we demonstrate that this cycle is present and then compare it with other examples in which a ~200-kyr cycle has been described in the literature, but which have a different origin and are not related to this weak eccentricity cycle. Finally, we aim to disentangle the exact origin of this cycle in terms of underlying g-frequencies.

2. Geological setting and sections

Along the north coast of Spain, lower Paleocene sediments are excellently exposed in coastal cliffs and consist of a rhythmic alternation of deep marine marls and limestones that were deposited in the Basque-Cantabrian Basin (Pujalte et al., 1995, 1998; Bernaola et al., 2006). The classical Zumaia section with its well-known Cretaceous/Paleogene (K/Pg) boundary is exposed west of the town of Zumaia in Basque country (Fig. 1). The section plays a crucial role in establishing an integrated magnetobiostratigraphic framework and astrochronology for the Paleocene and Maastrichtian, and bears the expression of the precession cycle in combination with ~100- and 405-kyr eccentricity (Dinarès-Turell et al., 2003, 2014; Kuiper et al., 2008; Westerhold et al., 2008; Batenburg et al., 2012, 2014). The manifestation of these cycles is not always perfectly clear as thin turbidites and associated colour changes disrupt the visual expression of the cycle pattern.

The parallel section of Hendaye is located just across the French border (Fig. 1). The Paleocene part of the succession is well exposed in the coastal cliffs situated northeast of Hendaye (see also Dinarès-Turell et al., 2013). The section covers the same interval of the Danian Limestone Formation and thus acts as a parallel section for Zumaia. An advantage of Hendaye is that the thin turbidites that are present at Zumaia and disrupt the cyclostratigraphy are (near) absent. As the coastal cliffs are (near-)vertical, pictures can be used for visual inspection and analysis of the cycle pattern, and for comparison with Zumaia (Fig. 2). For our cyclostratigraphic study, we used such pictures in combination with the high-resolution magnetic susceptibility and $CaCO_3$ records of Ten Kate and Sprenger (1993) generated for the same interval at Zumaia.

3. Cyclostratigraphic analysis

The rhythmically bedded marine marls and limestones of the Paleocene Danian Limestone Formation in the Zumaia and Hendaye sections reveal cyclicity at various scales (Dinarès-Turell et al., 2003). The basic sedimentary cycle consists of decimeter-thick alternations of reddish marl and whitish to pinkish limestone that have been attributed to precession (Fig. 2). These basic cycles are grouped in small-scale bundles of approximately 5 cycles, which mark the dominant cycle in the succession that is related to short ~100-kyr eccentricity (E-cycles of Dinarès-Turell et al., 2003; Fig. 2). In addition, larger-scale bundles have been identified that reflect the 405-kyr eccentricity cycle (Kuiper et al., 2008), while an even larger-scale cycle has been detected that marks the very long 2.0 Myr cycle (Dinarès-Turell et al., 2014). Finally, a weak expression of obliquity as distinctly thicker small-scale cycles may be seen in intervals in which short eccentricity related cycles become less prominent (E-cycles 12–15, and 28–30); such intervals may in addition correspond to minima (nodes) of the very long period eccentricity cycle, which result in a relatively stronger expression of obliquity.

3.1. Atypical cycle patterns

However, pictures of the steep coastal cliffs at Hendaye reveal an

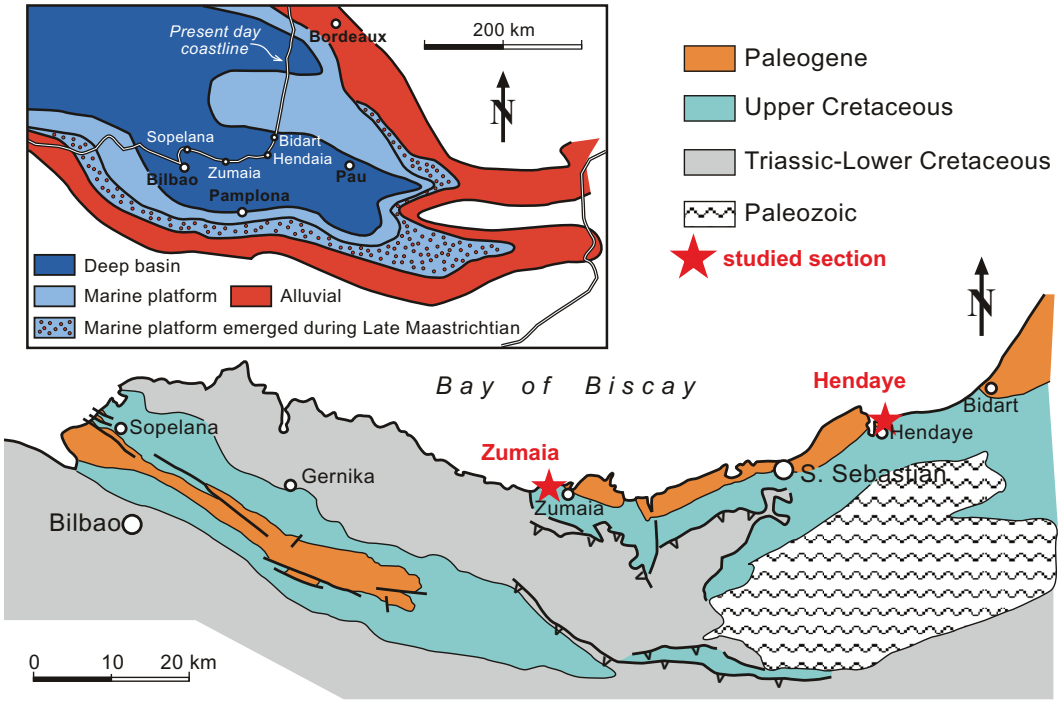

Fig. 1. Location map showing the locations of the Hendaye and Zumaia sections (slightly modified after Dinarès-Turell et al., 2013).

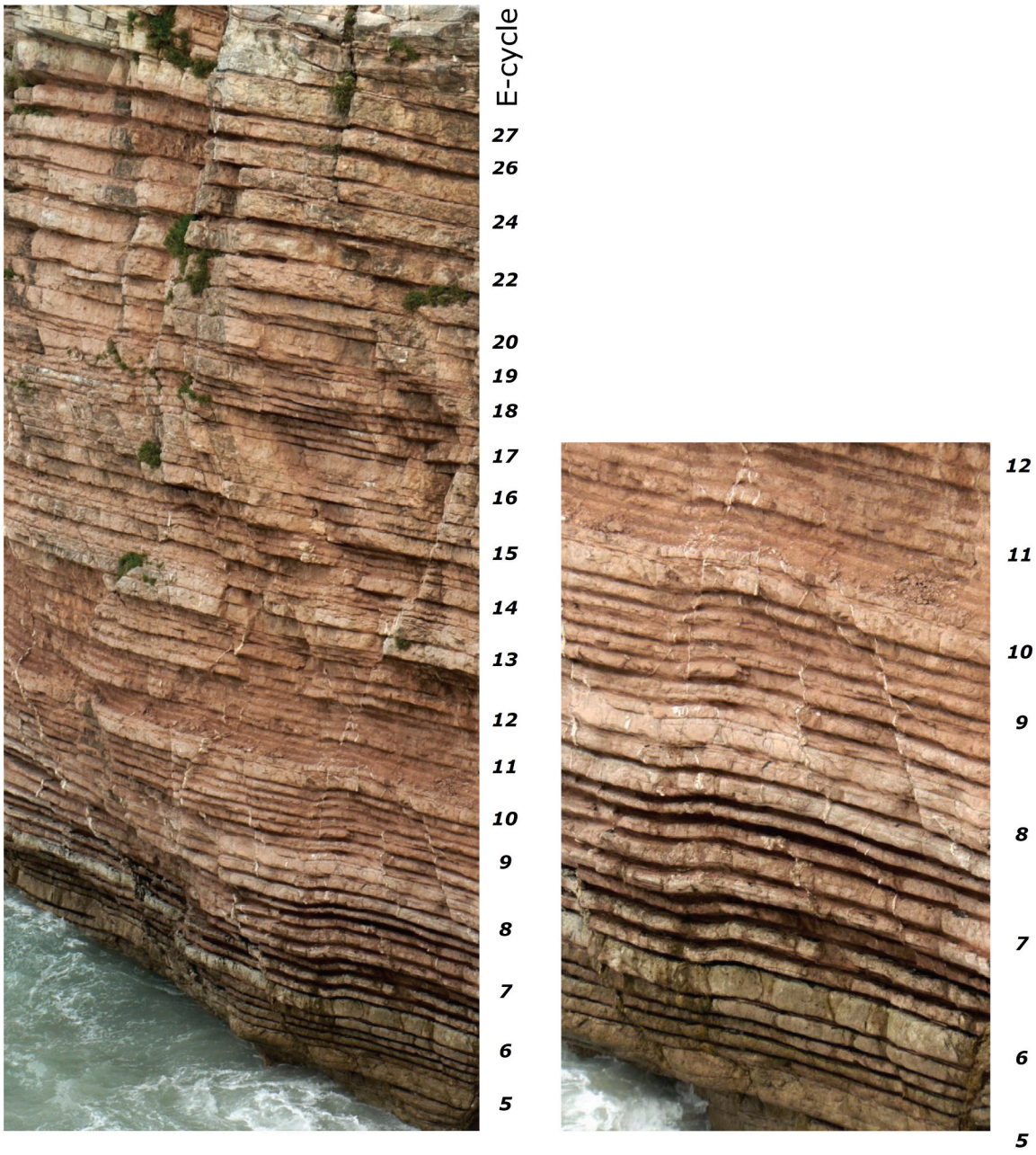

Fig. 2. Photographs of the rhythmically bedded marls and limestones of the lower Paleocene Danian Limestone Formation at Hendaye. A) Outcrop covering E-cycles 5 to 28 of Dinarès-Turell et al. (2003). B) Enlarged, showing E-cycles 5 to 12 with alternating strong and weak ~100-kyr carbonate maxima of cycles E6, E8, E10 and E12.

intriguing additional pattern with alternating prominent (E-cycles 6, 8, 10 and 12; see Fig. 2) and less prominent limestone beds associated with the inferred ~100-kyr cyclicity. Unfortunately, the section is too steep for easy sampling, but the same interval has been studied in the Zumaia section by Ten Kate and Sprenger (1993), who generated high-resolution $CaCO_3$ and magnetic susceptibility (MS) records of the lower 14 m of the Danian Limestone Formation directly above the K/Pg boundary. We did not include the data available for the ~60 m below this boundary because 1) depositional conditions are markedly different with much higher sedimentation rates and 2) the visual absence of such patterns both in outcrop and in the data of this interval. The records of the 14 m above the boundary are shown in Fig. 3 and provide the quantitative data for time series analysis and independent statistical validation of the observed cycle pattern.

The records reveal prominent peaks in $CaCO_3$ (minima) and MS (maxima) that are associated with the reddish marls of the basic precession-related cycles with an average thickness of ~25 cm, although the actual thickness ranges from 20 to more than 30 cm. These peaks can be grouped into the small- and large-scale bundles that reflect the ~100- and 405-kyr eccentricity-related cycles identified by Dinarès-Turell et al. (2003) and Kuiper et al. (2008); such bundles of well-developed small-scale precession related cycles correspond to eccentricity maxima, as eccentricity modulates the precession amplitude. The eccentricity related pattern becomes more easily visible in case an unweighted 7 point moving average is applied to the original records to remove the high frequency precession related variability (Fig. 3). The expression of the limestone beds of the ~100-kyr eccentricity related E-cycles of Dinarès-Turell et al. (2003) can easily be recognized (Fig. 3). The smoothed records in addition reveal a pattern of alternating distinct and less distinct $CaCO_3$ maxima and MS minima that corresponds

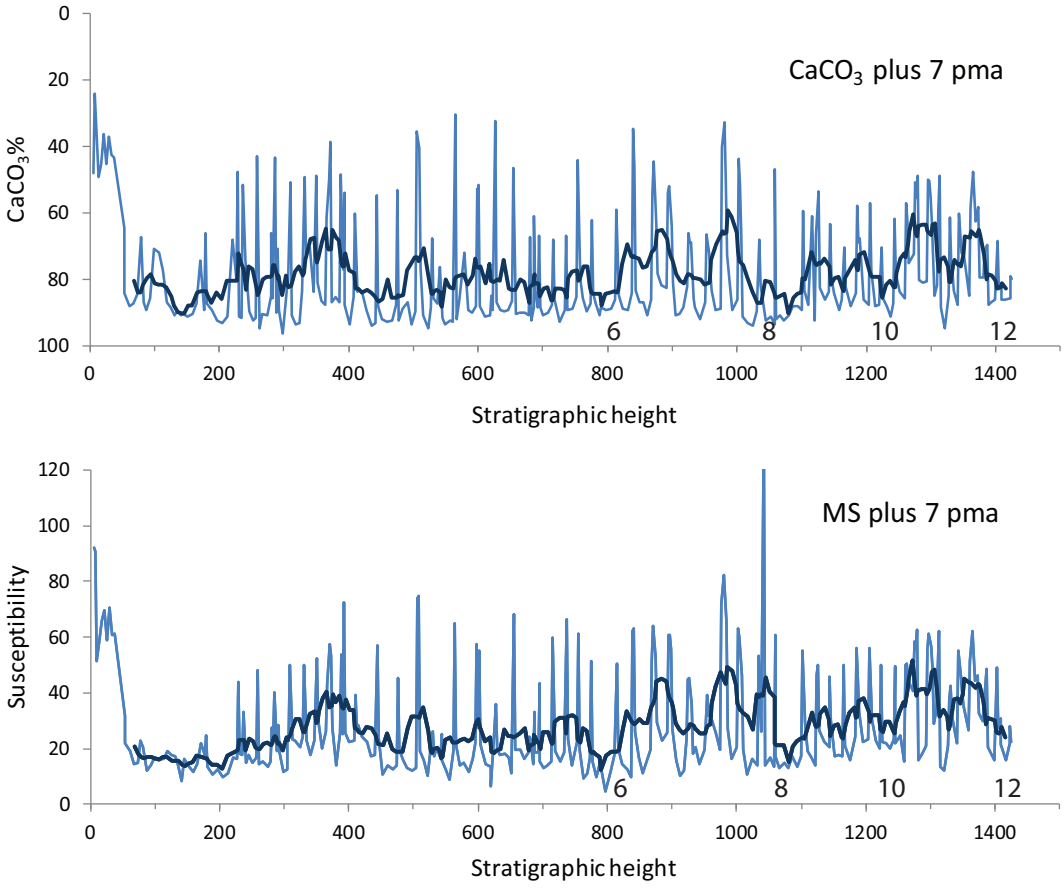

Fig. 3. Magnetic susceptibility (lower) and $CaCO_3$ (upper) records of the lower 14 m directly above the K/Pg boundary in the Zumaia section (from Ten Kate and Sprenger, 1993). Also shown are smoothed records based on unweighted 7 point moving averages. The basal part (~65 cm) is not used as it reflects the dark marl bed associated with the K/Pg boundary. The position of the limestone beds of the ~100-kyr E-cycles of Dinarès-Turell et al. (2003) are indicated with the prominent limestone beds of E-cycles 6, 8, 10 and 12 that are part of the intriguing and complex cycle pattern in bold.

to the alternating pattern of prominent and less prominent ~100-kyr E-cycle limestone beds seen at Hendaye in the field (Figs. 2 and 3). Finally, they show the low $CaCO_3$ content and high MS values of the dark marls associated with the K/Pg boundary (basal 40 cm).

3.2. Time series analysis using simple 100-kyr cycle age model

Time series analysis in the stratigraphic domain is complicated by the changes in sedimentation rate suggested by the variable thickness of the basic precession-related cycles. For this reason, we converted the quantitative records of Ten Kate and Sprenger (1993) to time, starting from an age of ~66 Ma for the K/Pg boundary, and assigning an age of 65.8 Ma to the mid-point of the limestone part of ~100-kyr eccentricity-related cycle E2 of Dinarès-Turell et al. (2003) and a duration of 100-kyr to each successive ~100-kyr cycle (E2 to E12, see Fig. 2, Table 1). To determine the position of these mid-points, we identified the limestone beds of the basic precession-related cycle that correspond most closely with the indurated parts of the ~100-kyr E-cycles of Dinarès-Turell et al. (2003) in the $CaCO_3$ and MS records of Ten Kate and Sprenger (1993). The resulting time series were detrended and the data of the basal part removed to avoid the influence of the 40 cm thick basal marl layer associated with the K/Pg boundary.

We then applied spectral analysis on the unsmoothed, interpolated and detrended $CaCO_3$ and MS time series, using the Redfit method of Schulz and Mudelsee (2002) and running it in a relatively high frequency mode (with the Ofac parameter set at 4) to increase the resolution in the low frequency eccentricity band of the spectrum. Both the $CaCO_3$ and MS spectrum reveal strong peaks in the precession frequency band, as expected (Fig. 4). In addition, three distinct peaks with periods of ~100, ~200 and ~ 400-kyr are observed in the low frequency eccentricity band of the spectra. Most spectral peaks reach significance levels higher than 90%, while more often they are above 95% or even 99% (Fig. 4).

Bandpass filtering was used to extract the three low frequency cycles from the $CaCO_3$ and MS time series (Fig. 5A,B). The filtered ~100- and 405-kyr components follow the ~100- and 405-kyr cycles previously identified in this part of the Zumaia section (Dinarès-Turell

Table 1
Position and age of tie-points. Each ~100-kyr limestone bed of Dinarès-Turell et al. (2003) was assigned an age (Age 1), starting from an age of 65.9 Ma for the midpoint of the limestones of cycle E1 and assigning 100-kyr younger ages to each successive E-cycle. Ages of tie-points based on the astronomical calibration to revised La2010d solution have also been given (Age 2).

Tiepoint	Position	Age 1 (Ma)	Age 2 (Ma)
E2	298.0	−65.8	−65.871
E3	418.0	−65.7	−65.761
E4	527.7	−65.6	−65.656
E5	685.7	−65.5	−65.578
E6	797.3	−65.3	−65.49
E7	943.4	−65.3	−65.385
E8	1073.3	−65.2	−65.275
E9	1175.4	−65.1	−65.191
E10	1231.0	−65.0	−65.119
E11	1315.2	−64.9	−65.011
E12	1415.8	−64.8	−64.898

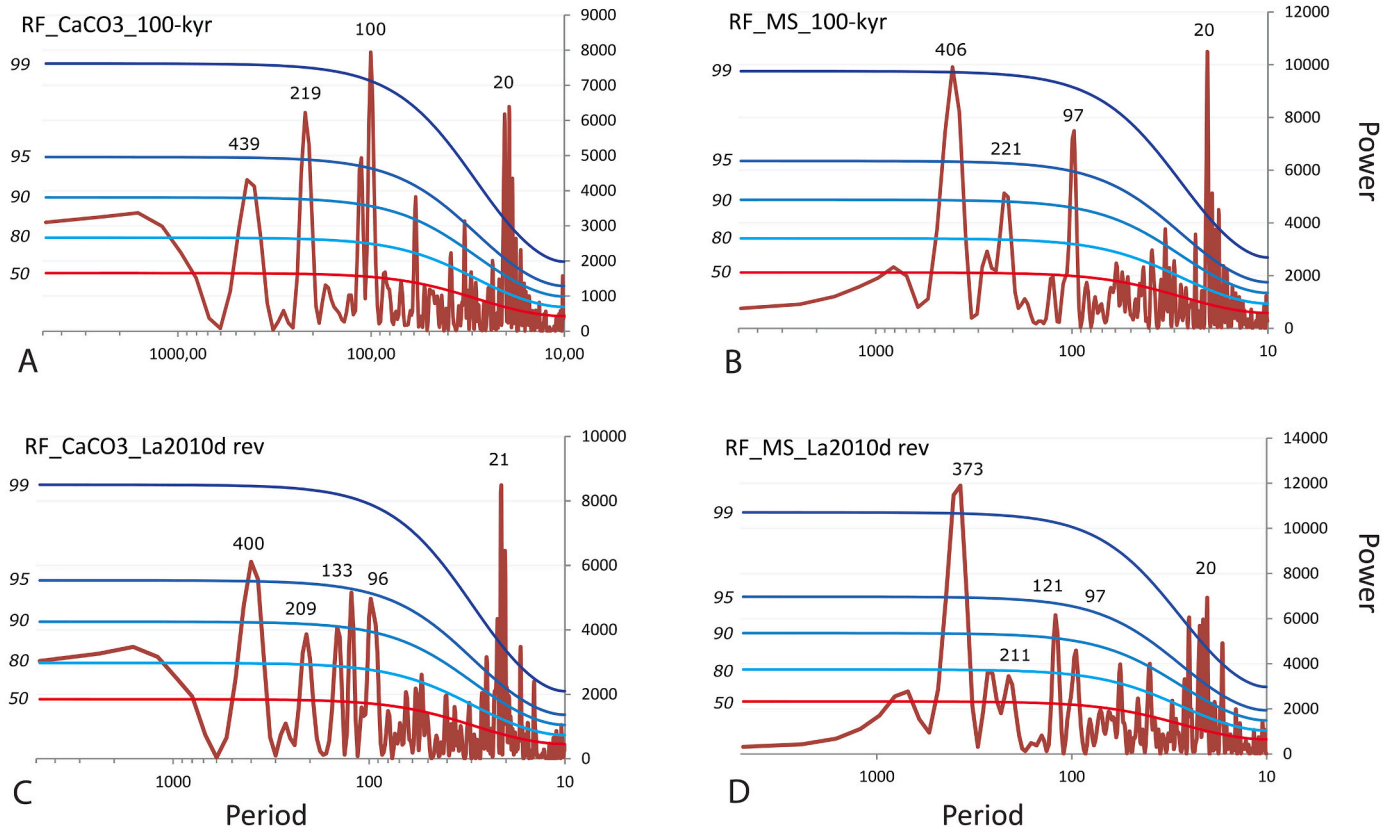

Fig. 4. Redfit spectra of the unsmoothed $CaCO_3$ and MS time series based on the 100-kyr age model (A-B) and the tuned age model (C-D). All spectra reveal strong peaks in the precession frequency band but also show three peaks in the eccentricity band with periods of ~100-, ~200- and 405-kyr. X-axis is shown on a logarithmic scale.

et al., 2003; Kuiper et al., 2008; Hilgen et al., 2010). The filtered ~200-kyr cycle tracks the alternating weak and strong $CaCO_3$ maxima and MS minima identified in the interval between 64.8 and 65.4 Ma in the time series, with prominent $CaCO_3$ maxima / MS minima at 64.8, 65.0, 65.2 and 65.4 Ma. It further closely follows the cycle pattern visually observed in the pictures of the Hendaye section (Fig. 2).

3.3. Application of an alternative tuned age model

We further tested the presence of the inferred ~200-kyr cycle by generating alternative time series of the proxy records for spectral analysis and bandpass filtering. This age model resulted from a separate attempt to reconstruct the eccentricity of the Earth's orbit for the entire time interval covered by the Danian Limestone Formation, using the visual expression of the sedimentary cycles at Hendaye and Zumaia. Here we used this reconstruction and the comparison with eccentricity time series to establish an astronomical tuning of the $CaCO_3$ and MS records on the short eccentricity scale. We only show the results based on the tuning to the La2010d revised solution marked by a constant ~2.4 Myr eccentricity cycle as it shows a very good to excellent fit with the eccentricity-related cycle patterns observed in the field and in the proxy records. The resulting spectra reveal essentially the same pattern as the spectra based on the 100-kyr cycle age model. Significance levels are mostly less high, especially for the ~100- and ~200-kyr cycles. Moreover, the ~100-kyr cycle is split up in two separate peaks with periods of approximately 100- and 130-kyr. This splitting can be expected to result from the tuning to 100-kyr eccentricity in the La2010d solution, resulting in a better partitioning of the main frequency components of this cycle (95/99 versus 124/132-kyr). Such frequency modulations are known from geological data (Huybers and Aharonson, 2010; Zeeden et al., 2015; Laurin et al., 2016). Bandpass filtering of the cycles and then especially the ~200-kyr cycle produced essentially the same results as for the 100-kyr age model (Fig. 5C). Astronomical ages of the selected tie-points for the tuning to La2010d revised have been added to Table 1. The eccentricity time series between 64 and 66 Ma based on the La2010d revised solution shows a remarkable good fit with the reconstructed eccentricity pattern and the bandpass filtered 200-kyr cycle component (Fig. 6).

Finally, we repeated the whole procedure, using different spectral techniques, as the Blackman-Tukey (BT), Maximum Entropy (ME), Periodogramme and MTM spectral analytical methods in Analyseries (Paillard et al., 1996), as well as amplitude demodulation techniques in the R 'astrochron package' (Meyers, 2014; R Develeopment Core Team, 2017) to test the robustness of the outcome of the time series analysis. In addition we carried out wavelet analysis, following the method of Torrence and Compo (1998) and Liu et al. (2007). The outcome of these tests are consistent with the results obtained earlier through Redfit and are included in the Supplementary Information.

4. Discussion

4.1. Explanations for ~200-kyr cycles observed in paleoclimatic records

This is not the first time that a cycle is detected in paleoclimatic records with a period of ~200-kyr. Such a cycle has previously been found by Beaufort (1994) in variations in wet bulk density and the abundance of the calcareous nannofossil *Coccolithus pelagicus* at ODP Site 747 in southern Indian Ocean. The most likely explanation for this cycle is the 173-kyr amplitude modulation of obliquity. This component results from the combination of the main ~41-kyr cycle component (related to p and s3) with the 54-kyr component (related to p and s6) and is thus related to s3-s6. Westerhold et al. (2005) similarly linked a

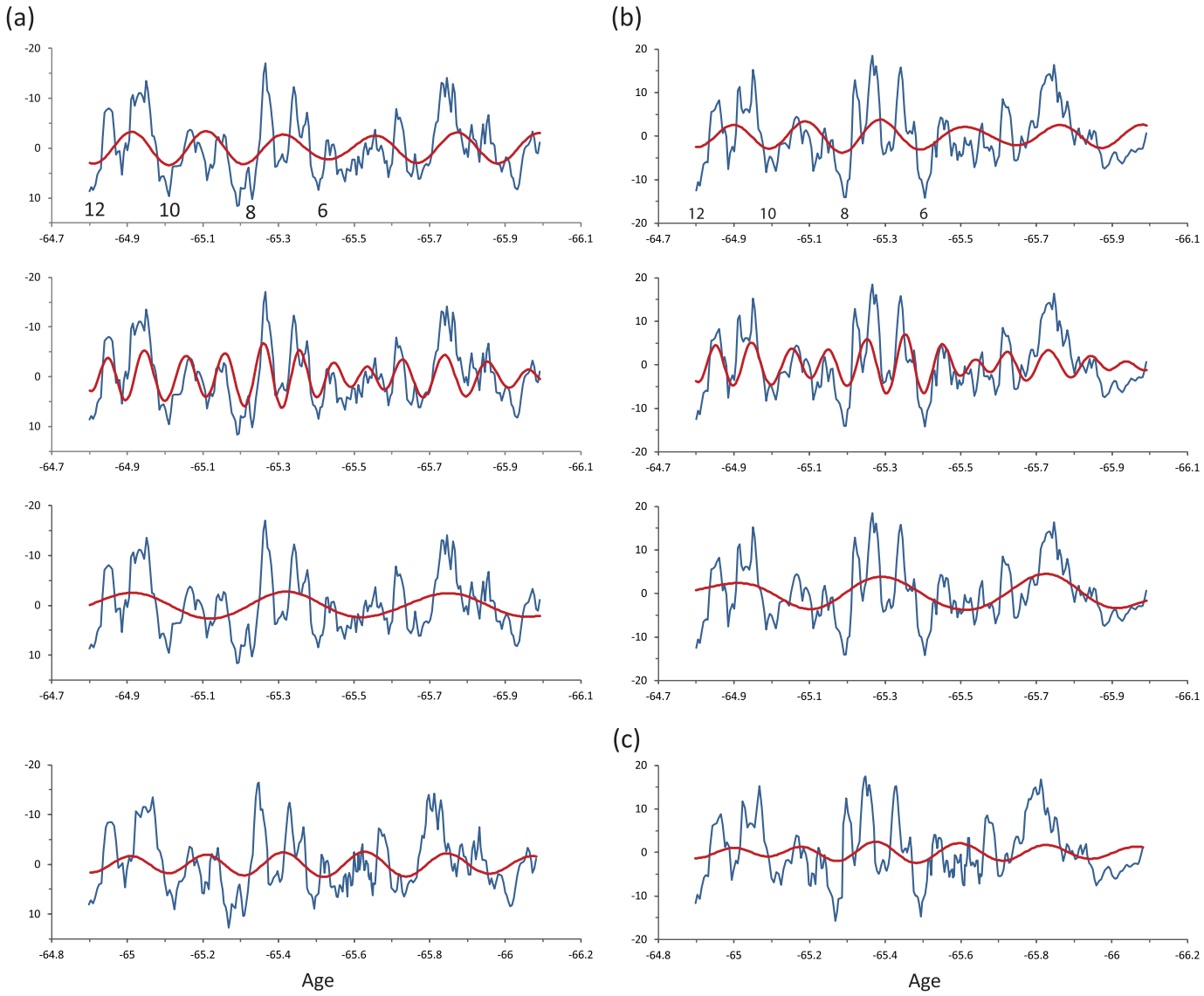

Fig. 5. Filtered ~200-kyr, ~100-kyr and ~400-kyr cycles from the detrended and smoothed $CaCO_3$ (A) and MS (B) time series based on the 100-kyr age model. Bandpass filter center frequencies and bandwidths are 0.005 ± 0.001 cycles/Myr for the ~200-kyr cycle, 0.01 ± 0.003 for the ~100-kyr cycle and 0.00285 ± 0.001 for the 405-kyr cycle. Also shown are the bandpass filtered ~200-kyr cycles from the La2010d tuned, detrended and smoothed $CaCO_3$ and MS time series (C), using a center frequency and bandwidth of 0.005 ± 0.0008 cycles/Myr.

180-kyr cycle in their middle to late Miocene $\delta^{18}O$ record of ODP Site 1085 from the SE Atlantic to this 173-kyr obliquity modulation cycle. The most unmistakable expression of this cycle has recently been found in middle Eocene carbonate-rich drift successions from the Newfoundland Ridge in the North Atlantic, which have been used to calibrate this interval of the astronomical time scale (Boulila et al., 2018). However, a similar origin for the ~200-kyr cycle at Zumaia and Hendaye is unlikely due to the weak expression of the basic 41-kyr obliquity in these sections, and the fact that the filtered component traces lithological cyclicity that is related to the short ~100-kyr eccentricity cycle.

A weak ~200-kyr cycle has also been detected in tuned benthic stable isotope records of late Oligocene - early Miocene age at Walvis Ridge Site 1264 in the SE Atlantic (Liebrand et al., 2016). This cycle either represents the ~180-kyr obliquity cycle or a harmonic of the 405-kyr cycle. However, such an harmonic is likely an artefact resulting from distortion of the initial sine wave of the forcing in the depth domain as a consequence of cycle asymmetry (i.e., threshold related or skewed form) or changes in sedimentation rate within the cycle. A ~ 200-kyr cycle has further been found in proxy records of the lowermost Paleocene of ODP Site 1209 (Hilgen et al., 2015), but in this case the cycle seems to result from a non-linear response to the astronomical forcing. Finally, results of wavelet analysis pointed to a 200-kyr cycle in the upper Cretaceous of the Tropical Atlantic Ocean (Friedrich et al., 2008). This cycle may signify a modification of the long or short eccentricity cycle, but more likely represents an artefact, resulting from a reduction in sedimentation rate by 50% that was not accounted for in the biostratigraphic age model (Friedrich et al., 2008).

At Zumaia and Hendaye, the good correspondence of the ~200-kyr cycle with the pattern in successive ~100-kyr $CaCO_3$ maxima and MS minima suggests that the ~200-kyr cycle does not represent the first harmonic of the 405-kyr cycle, which may enter the spectrum due to a non-linear response resulting in an asymmetric or skewed $CaCO_3$ cycle. As its expression as alternating (in)distinct limestone beds is reflecting eccentricity minima and not maxima, it is also less likely a double cycle of the ~100-kyr cycle, even though it correspond with two ~100-kyr cycles and, thus, results from interference with this ~100-kyr cycle.

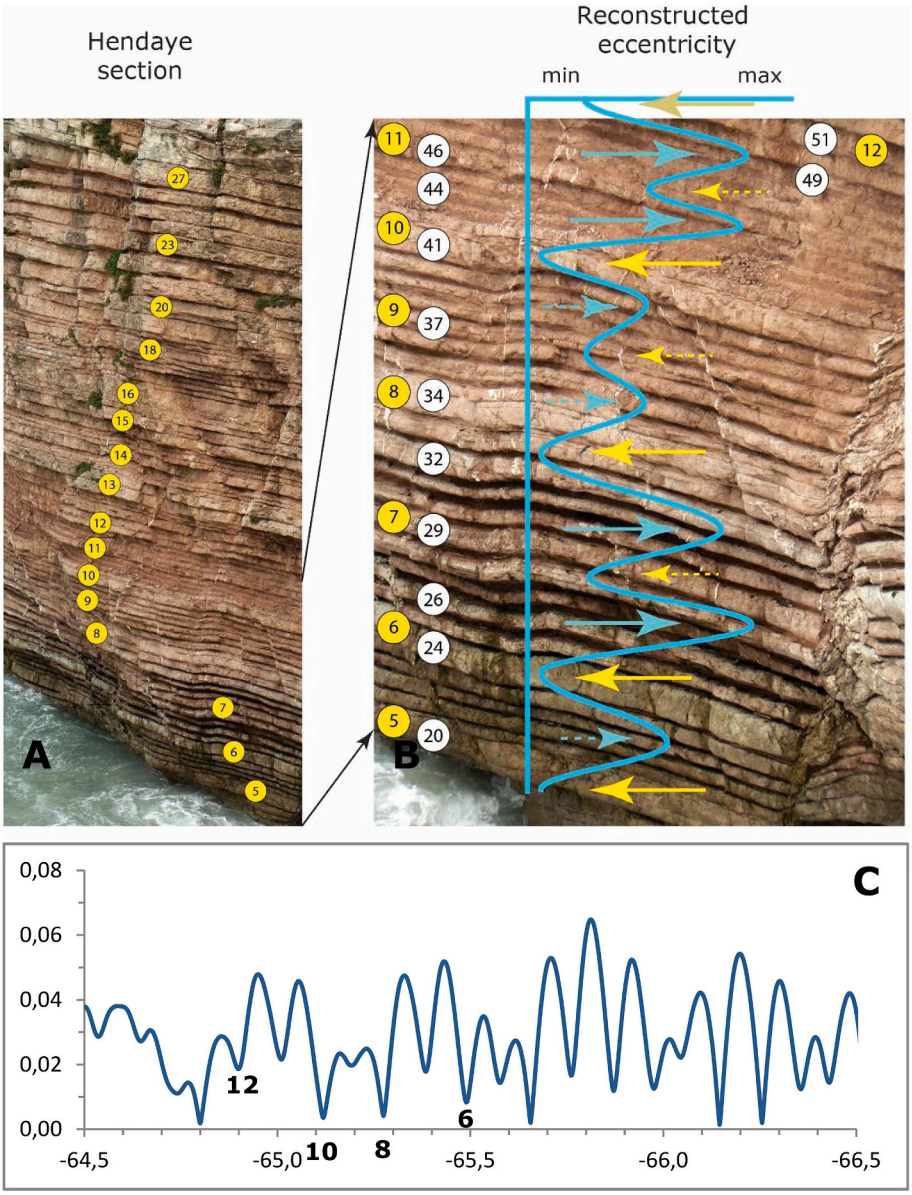

Fig. 6. Photographs of the lower Paleocene Danian Limestone Formation at Hendaye. A) Outcrop covering E-cycles 5 to 28 identified by Dinarès-Turell et al. (2003) at Zumaia. B) Enlarged, showing E-cycles 5 to 12 with alternating strong and weak ~100-kyr carbonate maxima (6, 8, 10 and 12) and reconstructed eccentricity on the basis of the cycle pattern and inferred phase relations (see running text). Numbers in white circles denote numbered small-scale cycles at the precession-scale identified by Dinarès-Turell et al. (2003) at Zumaia. Solid arrows mark strong eccentricity maxima (blue) and minima (orange) while dashed arrows mark weak maxima (blue) and minima (orange). C) Eccentricity time series between 64.5 and 66.5 Ma based on the revised La2010d solution with a stable 2.4 Myr cycle that shows a remarkable fit with the reconstructed cycle pattern. The tuning of the limestone beds of E-cycles 6, 8, 10 and 12, which represent the distinct beds in the alternatingly distinct and less distinct beds of the ~100-kyr eccentricity related cycle, is also indicated. (For interpretation of the references to colour in this figure legend, the reader is referred to the web version of this article.)

4.2. Alternative eccentricity explanation for the 200-kyr cycle at Zumaia and Hendaye

The most logical explanation for the observed ~200-kyr cycle is that it represents a weak but real frequency component of eccentricity. However, in that case, it is important to look into the corresponding frequency band of eccentricity to determine the origin of this cycle and its associated pattern of alternating strong and weak ~100-kyr eccentricity minima in detail. A ~200-kyr cycle in eccentricity has previously been identified by Hinnov (2000) in the amplitude and frequency modulations of precession, but its origin remained unexplained. The peak in the spectrum of Hilgen et al. (Hilgen et al., 2015; labelled 202-kyr) is relatively broad and composite, suggesting that it consists of more than just a single component. However, one may also argue that this peak embodies a modulating term of obliquity, as the figure does not show an eccentricity spectrum, but that of ETP (normalized eccentricity, tilt or obliquity and precession). However, this is unlikely as only obliquity is included in ETP and not its amplitude modulation separately, as is the case for the combination of precession and eccentricity.

Due to its weak expression, the ~200-kyr eccentricity cycle becomes clearer in case spectral power is depicted on a logarithmic scale. In fact, the power of this cycle is two orders weaker than that of the dominant components of the ~100-kyr cycle. Nevertheless, the ~200-kyr cycle is well expressed in eccentricity time series as alternating strong and weak minima of the ~100-kyr cycle, but only in specific intervals, likely as a consequence of interference with the ~100-kyr cycle. The fact that it is predominantly expressed in the minima and only very limited in the maxima is also explained by the weakness of this cycle. This weakness and the resultant expression in eccentricity time series further explains the difficulty in detecting this cycle in the geological archives, as the climate response is often non-linearly amplified in the direction of eccentricity maxima, as a consequence of the enhanced seasonal contrast associated with precession extremes and alternatingly experienced by each hemisphere. By contrast, this response often attains more uniform background values during ~100-kyr minima, also because there are no climatic thresholds to be passed.

The pattern observed in the eccentricity time series that is related to the ~200-kyr cycle is identical to that seen in our proxy records. However, this similarity critically depends on the inferred phase relation between the larger-scale eccentricity related cycles in the Zumaia-Hendaye sections and eccentricity itself, with $CaCO_3$ maxima and MS

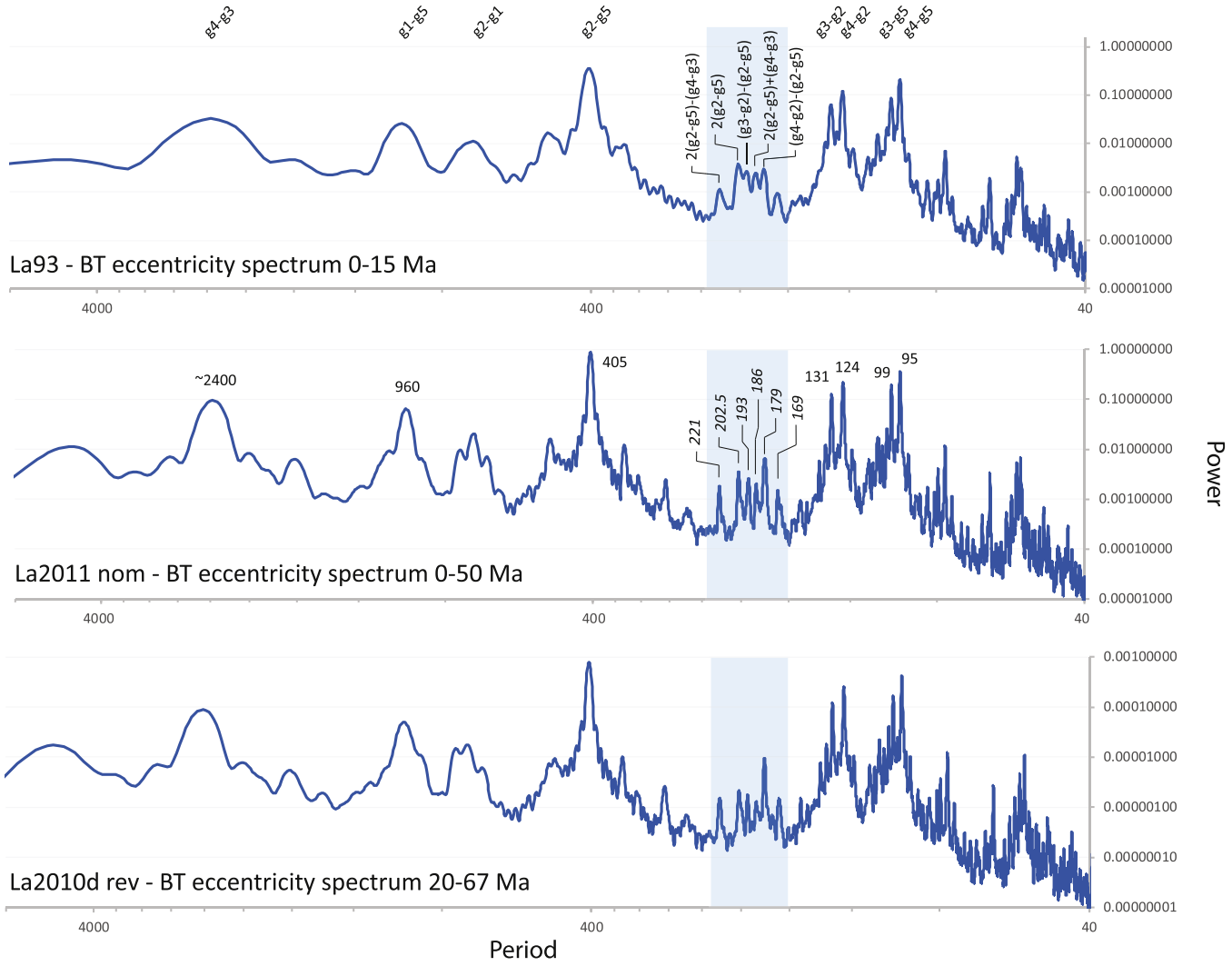

Fig. 7. High-resolution Blackman-Tukey spectra of eccentricity for the last 15 and 50 millions of years in the La93 and La2011 nominal solutions, respectively, and between 20 and 67 Ma in the La2010d revised solution.

minima corresponding to eccentricity minima, which has previously been used for the tuning of the Zumaia section (Dinarès-Turell et al., 2003; Kuiper et al., 2008). As mentioned before, this phase relation is based on the observation that the basic precession related cycles occur in groups of well-developed cycles with distinct reddish marls showing the expected 1:5:20 ratio between basic cycles and the larger-scale cycles of inferred eccentricity origin. In that case, it can safely be assumed that the bundles of distinct precession related cycles correspond to eccentricity maxima, as eccentricity determines the precession amplitude.

4.3. Origin of the ~200-kyr eccentricity cycle

To further check the presence of a ~200-kyr cycle in eccentricity, we generated high-resolution Blackman-Tukey spectra of eccentricity over the last 15 and 50 Myr for the La93 and La2011 nominal solutions (Laskar et al., 1993; Westerhold et al., 2012), respectively, and between 20 and 67 Ma for La2010d revised (Fig. 7). These time intervals are rather arbitrarily selected, but the solutions include the most recent La2011 nominal solution (Westerhold et al., 2012) and La2010d revised, which reveals such an excellent fit with the pertinent cycle pattern at that time. However, our approach is also designed to show that this elusive cycle is robustly present in different solutions and in different time intervals. The resultant spectra reveal a large number of very weak components with periods close to 200-kyr. Four components centered in the middle are somewhat stronger with periods of 179, 186, 193 and 202 kyr. Two additional peaks with slightly lower amplitudes are found just outside this band having periods of 168 and 221 kyr. We then applied narrow bandpass filtering to extract each of these components as well as a broader bandpass filter for the collective signal over the shared frequency band (Fig. 8). The individual components and the combined signal are shown as overlay on the eccentricity time series of the La2011 nominal solution for the interval between 5 and 7 Ma and of the revised La2010d solution for the interval between 64 and 66 Ma (Fig. 8). In these intervals, the combined signal convincingly tracks the characteristic pattern of alternating strong and weak ~100-kyr minima and inclusion of the 168 and 221-kyr components does not make much of a difference. Looking at the individual components, the expression of the ~200-kyr cycle can be explained by a combination of individual components acting largely in-phase and reinforcing each other. In fact, most of the individual ~200-kyr components are in-phase in the middle of the interval between 5 and 7 Ma for La2011 (especially from 5.6 to 5.9 Ma) and between 64 and 66 Ma for La2010d revised (especially from 65.0 to 65.5 Ma), where the ~200-kyr cycle is expressed as alternating strong and weak ~100-kyr eccentricity minima. However, the two ~200-kyr components that contribute most to the signal between 5 and 7 Ma in La2011 are the ones with periods of 179- and 193-kyr, while the two components that contribute most between

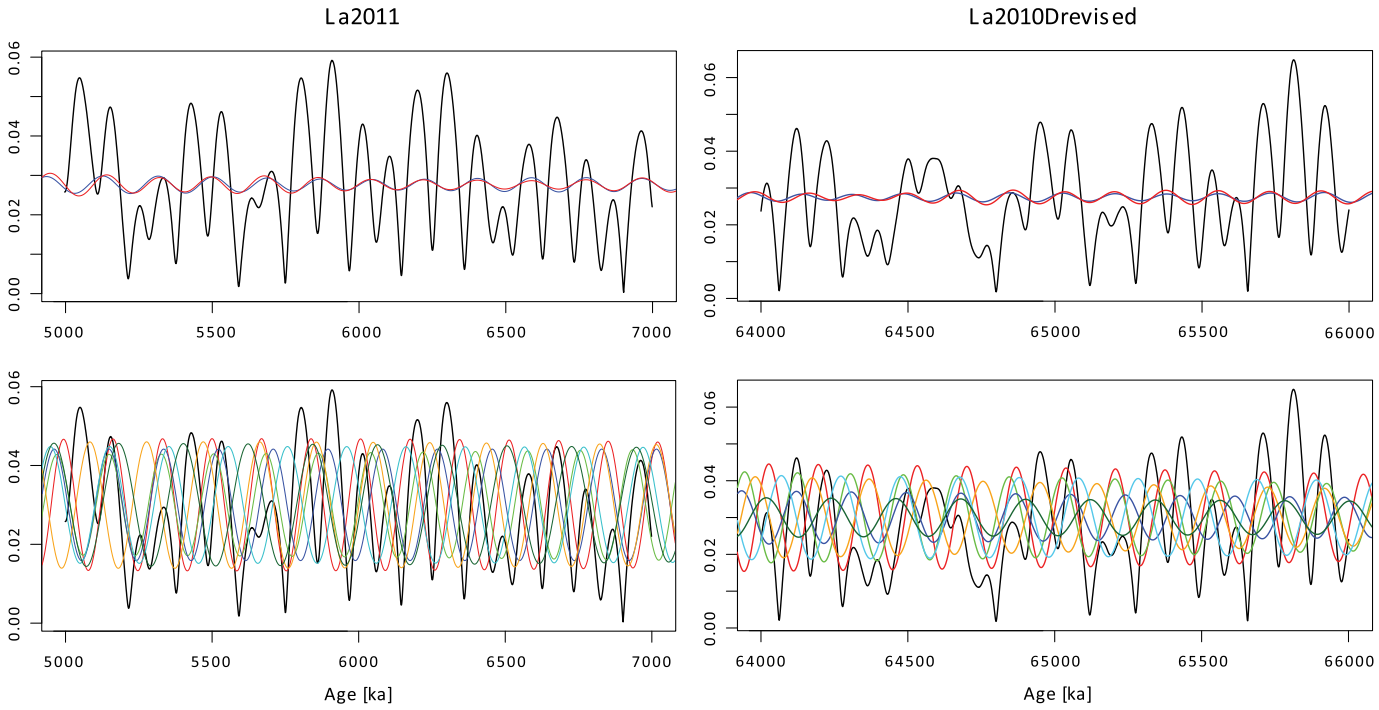

Fig. 8. Bandpass filtered 1/200 kyr frequency components in eccentricity between 5 and 7 Ma in the La2011 nominal solution (A) and between 64 and 66 Ma in the La2010d revised solution (B), using a Taner filter with roll = 10^50. In the upper panel, two broad filters were used with bandwidths of 0.004717–0.005747 (1/kyr, blue) and 0.004–0.006 (red), while narrow filters were used in the lower panel to extract all the 6 individual components in the ~200-kyr eccentricity band, using bandwidths of 0.005848–0.005988 (red), 0.005494–0.005618 (green), 0.005318–0.005382 (blue), 0.005103–0.005207 (orange), 0.004901–0.004901 (light blue) and 0.004505–0.004545 (dark green). (For interpretation of the references to colour in this figure legend, the reader is referred to the web version of this article.)

Table 2
The 5 identified eccentricity terms that are likely involved in our ~200-kyr cycle. Periods have been computed with the help of the La2004 and La2010a solutions, using the origin of the components in term of g-frequencies. Also the periods of the associated peaks in the La2010a spectrum, as shown in Fig. 7, are given.

TERM	La2004	La2010a	Spectrum
2(g2 – g5)	202.846	202.784	202/203
(g4 – g2) – (g2 – g5)	178.283	178.329	179
(g3 – g2) – (g2 – g5)	192.816	192.872	193
2(g2 – g5) – (g4 – g3)	221.873	221.803	221
2(g2 – g5) + (g4 – g3)	186.825	186.769	186

64 and 66 Ma in La2010d revised have periods of 168- and 179-kyr.

Evidently, the origin of the ~200-kyr cycle is complex as it is composed of 4 to 6 individual eccentricity components with periods varying between 179 (168) and 202 (222) kyr. Such components can be defined in terms of their frequency and phase, and ranked according to amplitude (e.g., Laskar et al., 2004; Laskar et al., 2011a; Hinnov, 2013). However, they can also be written in terms of their origin, namely as a combination of g-frequencies of different planets, while s-frequencies may be part of weaker components (Laskar et al., 2004; Hinnov, 2000). The principal eccentricity components invariably represent 2nd order terms which combine two g frequencies of the inner planets and Jupiter, as these exert the greatest gravitational influence on Earth. Initially combinations of the precessional motion of the perihelion (g frequencies) and/or nodes (s frequencies) of Venus and Neptune were thought to be responsible for the weak components of our ~200-kyr cycle, but the gravitational influence of Neptune on Earth is likely too small. Alternatively, it cannot be excluded that higher order terms which are composed of combinations of multiple g- and s-frequencies are involved. Hinnov (2000) mentions a 187.8 kyr cycle in the amplitude modulation of obliquity that she relates to s3 − g4 + g3 − s6. However, the period of this component, which may also show up in eccentricity, arrives at 161.080 kyr in case the same g- and s-frequencies of La2010a are used for its computation, which is well outside the range of the frequencies observed in the ~200-kyr band of our eccentricity spectra. By contrast, the combination s3 − g3 + g4 − s6 produces a period of 186.441 kyr in La2010a, and might be responsible for the 186-kyr peak observed in our eccentricity spectra (Fig. 7). However, this is also not likely as s-frequencies are involved, which exert much less influence on eccentricity than g frequencies. This is confirmed by results of spectral analysis of a simplified eccentricity solution, which is based only on the 5 most important g-frequencies g1 to g5 (Laskar, 2020). The resultant spectrum is similar to that of the full solution and reveals that almost all of the 4 to 6 components involved in our ~200-kyr cycle must be related to combinations of these five g frequencies. Further study revealed that they correspond to higher order terms. Three of them have now been identified as 4th order terms (g4 – g2) – (g2 – g5) (178 kyr, period computed with the help of La2010a, see Table 2), (g3 – g2) – (g2 – g5) (193) and 2(g2 – g5) (202/203) and two as 6th order terms 2(g2 – g5) – (g4 – g3) (222) and 2(g2 – g5) + (g4 – g3) (187), representing the real harmonic, 2(g2 – g5), of the 405-kyr cycle and related terms. The two 6th order terms were previously mentioned in Berger and Loutre (1990). These 5 components all represent combinations of 2nd order terms and are written in such a way as to clarify their derivation. The weak 168 kyr component is more involved, as it is not unambiguously related to a single frequency combination. The weakness of all 5 identified components with amplitudes approximately two orders lower than the leading terms underlying the main eccentricity cycles are explained by the fact that they are related to higher order terms and not to second order terms associated with a combination of 2 main g frequencies, as are the 405-kyr cycle and the 4 dominant ~100-kyr components. However, it should be realized that the expression of – the combined influence of – these weak components is only possible because they are not overwhelmed by much stronger 2nd order terms in this specific

frequency band of the eccentricity spectrum. It is for the first time that the influence of such weak higher order components is identified in paleoclimatic records. Finally, the characteristic pattern that results from interference with the much stronger ~100-kyr cycle might be used as a template for testing the accuracy of astronomical solutions in the future.

4.4. Applications

The pattern in the eccentricity time series of La2010d revised between 64 and 66 Ma is very characteristic and, as mentioned before, in excellent agreement with the observed sedimentary cycle pattern. Such a pattern can in principle be used to discriminate between astronomical solutions and ascertain which one is reliable for this time interval. The main problem with the astronomical solution is the chaotic behavior of the Solar System, which currently limits the reliability of the solution back to ~50 Ma (Laskar et al., 2011a; Westerhold et al., 2012) and ultimately to 60 Ma (Laskar et al., 2011b). As a result, the only option to extend the solution further back in time is through a detailed comparison with cyclostratigraphy. The observed pattern, especially in combination with locating the nodes of the very long ~2.0 Myr cycle could be very useful for that purpose. The origin of most of the higher order components that together constitute our ~200-kyr cycle depend on g2 and g5 and the combination of these two is stable (reason why the 405-kyr long eccentricity cycle, being associated with g2 – g5, is so stable). However, other components of the ~200-kyr cycle also include g3 and g4, which are involved in the chaotic behavior through the resonance term (g4 – g3) − 2(s4 – s3) = 0 with g4 – g3 being responsible for the present-day ~2.4 Myr cycle. As a result, the ~200-kyr cycle pattern will also change as a consequence of the chaotic behavior of the Solar System and the chaotic drift in the fundamental frequencies g3 and g4. It can thus probably be used to assess the "correctness" of astronomical solutions. The procedure to be followed will include the generation of many different solutions by making small changes in the "initial conditions" of the solution. It should be realized that the excellent agreement between La2010d revised and the intricate cycle pattern related to the ~200-kyr cycle does by no means imply that this solution is the correct one for all time as the agreement might be caused by coincidence. A full study should include the entire interval from 50 to 66 Ma. In fact, a quick comparison of this specific solution with the cycle pattern between 50 and 58 Ma shows that this La2010d modified solution is likely not the most relevant solution for this time interval and thus that the ~2.4 Myr cycle is not constant (see also Zeebe and Lourens, 2019).

Finally one can ask the question why the discovery of this new cycle in the stratigraphic record is important from a paleoclimatic point of view especially since it is so weak and remained undetected for so long in the many high-resolution climate proxy records that were available. In that respect, it looks like an odd finding, but it tells us that the climate system is apparently sensitive enough to respond to the small insolation changes that are connected with this cycle. In fact, these changes are associated with precession as eccentricity acts as amplitude modulator of precession, which is its main influence. Apart from its weakness, another reason that this cycle has not been observed before is that the climate system often responds in a non-linear way to the insolation changes and, hence, that subtle differences between successive ~100-kyr minima are further suppressed and remain undetected.

5. Conclusions

For the first time, the expression of a weak ~200-kyr Milankovitch cycle has been detected in the lower part of the Danian Limestone Formation as exposed in the Zumaia and Hendaye sections. This cycle is clearly expressed as alternating distinct and less distinct $CaCO_3$ maxima and associated MS minima which by themselves are related to eccentricity minima associated with the dominant ~100-kyr cycle.

The observed cycle does not represent the 173-kyr obliquity cycle, nor an artificial harmonic of the 405-kyr cycle or a double ~100-kyr cycle that may result from a non-linear response of the climate system to the astronomical forcing. In fact, it most probably reflects a real but weak and complex eccentricity component that is related to higher 4th and 6th order terms in eccentricity, in contrast to the much stronger 2nd order terms that underlie the principal eccentricity cycles.

Declaration of Competing Interest

Please check the following as appropriate:

All authors have participated in (a) conception and design, or analysis and interpretation of the data; (b) drafting the article or revising it critically for important intellectual content; and (c) approval of the final version.

This manuscript has not been submitted to, nor is under review at, another journal or other publishing venue.

The authors have no affiliation with any organization with a direct or indirect financial interest in the subject matter discussed in the manuscript.

Acknowledgements

CZ has been supported by a PSL fellowship. JL is supported by the ANR AstroMeso. Two anonymous reviewers are thanked for helpful comments that improved the manuscript.

References

Batenburg, S.J., Sprovieri, M., Gale, A.S., Hilgen, F.J., Hüsing, S., Laskar, J., Liebrand, D., Lirer, F., Orue-Etxebarria, X., Pelosi, N., Smit, J., 2012. Cyclostratigraphy and astronomical tuning of the late Maastrichtian at Zumaia (Basque country, Northern Spain). Earth Planet. Sci. Lett. 359-360, 264–278.

Batenburg, S.J., Gale, A.S., Sprovieri, M., Hilgen, F.J., Thibault, N., Boussaha, M., Orue-Etxebaria, X., 2014. An astronomical time scale for the Maastrichtian based on the Zumaia and Sopelana sections (Basque country, northern Spain). J. Geol. Soc. 171, 165–180. https://doi.org/10.1144/jgs2013-015.

Beaufort, L., 1994. Climatic importance of the modulation of the 100 kyr cycle inferred from 16 m.y. long Miocene records. Paleoceanography 9, 821–834.

Berger, A.L., Loutre, M.-F., 1990. Origine des fréquences des éléments astronomiques intervenant dans le calcul de l'insolation. Bull. Classe Sci. Acad. Roy. Belg. 6e serie 1, 45–106.

Bernaola, G., Baceta, J.I., Payros, A., Orue-Etxebarria, X., Apellaniz, E., 2006. The Paleocene and lower Eocene of the Zumaia section (Basque Basin). In: Climate and Biota of the Early Paleogene 2006. Post Conference Field Trip Guidebook, Bilbao, pp. 82.

Boulila, S., Vahlenkamp, M., De Vleeschouwer, D., Laskar, J., Yamamoto, Y., Pälike, H., Kirtland Turner, S., Sexton, P.F., Westerhold, T., Röhl, U., 2018. Towards a robust and consistent middle Eocene astronomical timescale. Earth Planet. Sci. Lett. 486, 94–107.

Dinarès-Turell, J., Baceta, J.I., Pujalte, V., Orue-Etxebarria, X., Bernaola, G., Lorito, S., 2003. Untangling the Palaeocene climatic rhythm: an astronomically calibrated early Palaeocene magnetostratigraphy and biostratigraphy at Zumaia (Basque basin, northern Spain). Earth Planet. Sci. Lett. 216, 483–500.

Dinarès-Turell, J., Pujalte, V., Stoykova, K., Elorza, J., 2013. Detailed correlation and astronomical forcing within the Upper Maastrichtian succession in the Basque Basin. Bol. Geol. Min. 124, 253–282.

Dinarès-Turell, J., Westerhold, T., Pujalte, V., Röhl, U., Kroon, D., 2014. Astronomical calibration of the Danian stage (early Paleocene) revisited: Settling chronologies of sedimentary records across the Atlantic and Pacific Oceans. Earth Planet. Sci. Lett. 405, 119–131. https://doi.org/10.1016/j.epsl.2014.08.027.

Friedrich, O., Norris, R.D., Bornemann, A., Beckmann, B., Pälike, H., Worstell, P., Hofmann, P., Wagner, T., 2008. Cyclic changes in Turonian to Coniacian planktic foraminiferal assemblages from the tropical Atlantic Ocean. Mar. Micropaleontol. 68, 299–313.

Hilgen, F.J., Kuiper, K.F., Lourens, L.J., 2010. Evaluation of the astronomical time scale for the Paleocene and earliest Eocene. Earth Planet. Sci. Lett. 300, 139–151. https://doi.org/10.1016/j.epsl.2010.09.044.

Hilgen, F.J., Abels, H.A., Kuiper, K.F., Lourens, L.J., Wolthers, M., 2015. Towards a stable astronomical time scale for the Paleocene: aligning Shatsky Rise with the Zumaia – Walvis Ridge ODP site 1262 composite. Newsl. Stratigr. 48, 91–110. https://doi.org/10.1127/nos/2014/0054.

Hilgen, F.J., Hinnov, L.A., Aziz, H.A., Abels, H.A., Batenburg, S., Bosmans, J.H.C., de Boer, B., Hüsing, S.K., Kuiper, K.F., Lourens, L.J., Rivera, T., Tuenter, E., van de Wal, R.S.W.V., Wotzlaw, J.-F., Zeeden, C., 2015a. Stratigraphic continuity and fragmentary sedimentation: the success of cyclostratigraphy as part of integrated

stratigraphy. Geol. Soc. Lond. Spec. Publ. 404, SP404.12. https://doi.org/10.1144/SP404.12.
Hinnov, L.A., 2000. New perspectives on orbitally forced stratigraphy. Annu. Rev. Earth Planet. Sci. 28, 419–447. https://doi.org/10.1146/annurev.earth.28.1.419.
Hinnov, L.A., 2013. Cyclostratigraphy and its revolutionizing applications in the Earth and Planetary Sciences. Geol. Soc. Am. Bull. 125, 1703–1734 125th Anniversary Volume.
Huybers, P., Aharonson, O., 2010. Orbital tuning, eccentricity, and the frequency modulation of climatic precession. Paleoceanography 25. https://doi.org/10.1029/2010PA001952.
Kuiper, K.F., Deino, A., Hilgen, F.J., Krijgsman, W., Renne, P.R., Wijbrans, J.R., 2008. Synchronizing the Rock Clocks of Earth history. Science 320, 500–504.
Laskar, J., 2020. Cyclostratigraphy and astrochronology. In: Gradstein, F.M. (Ed.), The Geologic Time Scale 2020. Elsevier Publ. Comp.
Laskar, J., Joutel, F., Boudin, F., 1993. Orbital, precessional and insolation quantities for the Earth from −20 Myr to + 10 Myr. Astron. Astrophys. 270, 522.
Laskar, J., Robutel, P., Joutel, F., Gastineau, M., Correia, A.C.M., Levrard, B., 2004. A long term numerical solution for the insolation quantities of the Earth. Astron. Astrophys. 428, 261–285.
Laskar, J., Fienga, A., Gastineau, M., Manche, H., 2011a. La2010: a new orbital solution for the long-term motion of the Earth. Astron. Astrophys. 532, A89. https://doi.org/10.1051/0004-6361/201116836.
Laskar, J., Gastineau, M., Delisle, J.-B., Farrés, A., Fienga, A., 2011b. Strong chaos induced by close encounters with Ceres and Vesta. Astron. Astrophys. 532. https://doi.org/10.1051/0004-6361/201117504.
Laurin, J., Meyers, S.R., Galeotti, S., Lanci, L., 2016. Frequency modulation reveals the phasing of orbital eccentricity during Cretaceous Oceanic Anoxic event II and the eocene. Earth Planet. Sci. Lett. 442, 143–156.
Liebrand, D., Beddow, H.M., Lourens, L.J., Pälike, H., Raffi, I., Bohaty, S.M., Hilgen, F.J., Saes, M.J.M., Wilson, P.A., van Dijk, A.E., Hodell, D.A., Kroon, D., Huck, C.E., Batenburg, S.J., 2016. Cyclostratigraphy and eccentricity tuning of the early Oligocene through early Miocene (30.1-17.1 Ma): *Cibicides mundulus* stable oxygen and carbon isotope records from Walvis Ridge Site 1264. Earth Planet. Sci. Lett. 450, 392–405.
Liu, Y., San Liang, X., Weisberg, R.H., 2007. Rectification of the bias in the wavelet power spectrum. J. Atmos. Ocean. Technol. 24, 2093–2102.
Meyers, S.R., 2014. Astrochron: An R Package for Astrochronology Version 0.6.5.
Milankovitch, M., 1941. Kanon der Erdbestrahlungen und Seine Anwendung auf das Eiszeitenproblem. 132 Royal Serb. Sci. Spec. Publ., Belgrade.
Paillard, D., Labeyrie, L., Yiou, P., 1996. Macintosh program performs time-series analysis. Eos 77, 379.
Pujalte, V., Baceta, J.I., Dinarès-Turell, J., Orue-Etxebarrie, X., Parès, J.M., Payros, A., 1995. Biostratigraphic and magnetostratigraphic intercalibration of late Maastrichtian and Paleocene depositional sequences from the deep-water Basque basin, W Pyrenees, Spain. Earth Planet. Sci. Lett. 136, 17–30.
Pujalte, V., Baceta, J.I., Orue-Etxebarria, X., Payros, A., 1998. Paleocene strata of the Basque Country, western Pyrenees, northern Spain: facies and sequence development in a deep-water starved basin. In: de Graciansky, P.C.H., Hardenbol, J., Jacquin, T., Vail, P. (Eds.), Mesozoic and Cenozoic Sequence Stratigraphy of European Basins. 60. SEPM Spec. Publ., pp. 311–325.
R Develeopment Core Team, 2017. R: A Language and Environment for Statistical Computing. http://r-project.org.
Schulz, M., Mudelsee, M., 2002. REDFIT: estimating red-noise spectra directly from unevenly spaced paleoclimatic time series. Comput. Geosci. 28, 421–426.
Ten Kate, W.G., Sprenger, A., 1993. Orbital cyclicities above and below the Cretaceous-paleogene boundary at Zumaya (N Spain), Agost and Relleu (SE Spain). Sediment. Geol. 87, 69–101.
Torrence, C., Compo, G.P., 1998. A Practical Guide to Wavelet Analysis. Bull. Am. Meteorol. Soc. 79, 61–78.
Westerhold, T., Bickert, T., Röhl, U., 2005. Middle to late Miocene oxygen isotope stratigraphy of ODP site 1085 (SE Atlantic): new constrains on Miocene climate variability and sea-level fluctuations. Palaeogeogr. Palaeoclimatol. Palaeoecol. 217, 205–222. https://doi.org/10.1016/j.palaeo.2004.12.001.
Westerhold, T., Röhl, U., Raffi, I., Fornaciari, E., Monechi, S., Reale, V., Bowles, J., Evans, H.F., 2008. Astronomical calibration of the Paleocene time. Palaeogeogr. Palaeoclimatol. Palaeoecol. 257, 377–403.
Westerhold, T., Röhl, U., Laskar, J., 2012. Time scale controversy: accurate orbital calibration of the early Paleogene. Geochem. Geophys. Geosyst. 13. https://doi.org/10.1029/2012gc004096.
Zeebe, R.E., Lourens, L.J., 2019. Solar system chaos and the Paleocene–Eocene boundary age constrained by geology and astronomy. Science 365, 926–929. https://doi.org/10.1126/science.aax0612.
Zeeden, C., Meyers, S.R., Lourens, L.J., Hilgen, F.J., 2015. Testing astronomically tuned age models. Paleoceanography 30, 2014PA002762. https://doi.org/10.1002/2014PA002762.